Multispectral Drone-in-a-box System – Geometric System Calibration and Validation

Niko Koivumäki [1], Juha Suomalainen[1], Teemu Hakala[1], Eija Honkavaara[1]

[1] Finnish Geospatial Institute in National Land Survey of Finland, Vuorimiehentie 5, FIN-02150 Espoo, Finland –
niko.koivumaki@nls.fi, juha.suomalainen@nls.fi, teemu.hakala@nls.fi, eija.honkavaara@nls.fi

Keywords: Autonomy, Calibration, Direct georeferencing, Docker, Monitoring, Multispectral

Abstract

Drone-in-a-Box (DiaB) systems provide an automated remote sensing solution by integrating uncrewed aerial systems (UAS) with weather-resistant docking stations and cloud-based data processing. This architecture enables continuous operation, automated mission execution, and the generation of near real-time data products through combined onboard and cloud-based workflows. This offers significant new potential across a wide range of applications, including environmental monitoring, infrastructure inspection, emergency response, sustainable forestry, and precision agriculture. The objective of this study was to calibrate and evaluate the geometric performance of a novel multispectral DiaB system. A primary geometric processing pipeline was implemented, incorporating high-precision GNSS/IMU-based positioning and rigorous system calibration. The system's performance was assessed in controlled test field conditions and in operational forestry environment. The results demonstrated that the system was capable of achieving cm-level geometric accuracy and reliable photogrammetric processing without the use of *in situ* ground control points when bundle block adjustment is applied. Direct georeferencing provided dm-level accuracy. The findings indicate that the proposed system enables efficient and reliable data acquisition, while current limitations of its fully autonomous use are primarily related to data transfer constraints affecting real-time processing capabilities.

1. Introduction

Uncrewed Aerial Systems (UAS, drones) are advancing toward higher levels of autonomy, enabling remote operations and Beyond Visual Line of Sight (BVLOS) missions without onsite personnel. This transition is supported by several technological developments, including advances in autonomous flight control, communication systems, and cloud-based data processing. Among these, Drone-in-a-Box (DiaB) systems represent one practical approach, combining a weather-protected docking station with an autonomous aircraft and integrated management software.

A typical DiaB configuration includes five major components: (i) an intelligent ground station for hosting, charging, and protecting the aircraft; (ii) an autonomous drone capable of automatic take-off, landing, and data capture; (iii) a management unit for flight scheduling and system supervision; (iv) a communication network enabling command-and-control and data transfer; and (v) a cloud or server environment for data storage and analysis. Together, these components support high-frequency, scalable, and reliable aerial data acquisition.

DiaB systems open new opportunities across a wide range of applications, including long-term environmental monitoring, infrastructure inspection, security operations, emergency response, and decision support in domains such as forest management and precision agriculture. However, they simultaneously raise open questions related to BVLOS regulation, connectivity reliability, system standardization, and integration into existing operational workflows.

A critical requirement in monitoring applications is automated, high-precision georeferencing. While direct georeferencing (Schwarz et al., 1993) provides an efficient alternative for data processing, it remains constrained by technical limitations and system vulnerabilities (Nex et al., 2022; Alexandre et al., 2023). For achieving the highest precision, photogrammetric structure-from-motion (SfM) processing remains the preferred approach. However, this method is computationally intensive, relying on bundle block adjustment, dense point cloud generation, and orthorectification, most of which still depend on desktop-based post-processing (Jiang et al., 2020; Cheng et al., 2022).

Several approaches offer potential for improving processing efficiency. Cloud-based processing offers scalable alternatives; for example, La Salandra et al. (2024) proposed a distributed photogrammetric workflow using high-performance computing (HPC) clusters and open-source software, significantly reducing processing times through parallel computing, GPU acceleration, and hybrid bundle adjustment. This approach enabled near real-time delivery of critical geospatial data for emergency response. In addition, sequential processing approaches offer interesting alternatives for efficient processing (Hinzmann et al., 2018, Cheng et al., 2022). Across all approaches, high-performance GNSS/IMU systems and accurate system calibration remain key enablers for efficient and high-quality processing, both in direct georeferencing and bundle adjustment-based workflows.

The objective of this study was to implement a primary geometric processing pipeline for a novel multispectral DiaB system and to evaluate its geometric performance. Accurate geometry and operational efficiency are essential prerequisites for reliable monitoring outcomes. To meet these requirements, the system design incorporates a high-precision GNSS/IMU unit and rigorous geometric calibration procedures. In this study, the primary application focus of the system is high-accuracy forest monitoring missions.

2. Materials and methods

2.1 DiaB system

The DiaB system is based on the Rumble Tools Skynest platform equipped with a customised KB-Drone quadcopter (Rumble Tools Oy, Imatra, Finland). The UAV has a maximum take-off weight of 10 kg and dimensions of 51 cm x 55 cm x 30 cm (Figure 1). It has a downward looking camera for automatic landing. The Skynest system has a rugged, weather-resistant dock/box for housing the UAV and its sensor payloads. The box

https://doi.org/10.5194/isprs-archives-XLIX-B2-2026-1161-2026

provides integrated power management, ensuring continuous operation of both sensors and onboard electronics during flight. The Skynest KB DiaB can stream data in real time to cloud-based servers via a 4G mobile communications network, enabling continuous monitoring, mission management, and automated data upload.

The sensor payload includes a Micasense Altum-PT (AGEagle Aerial Systems Inc., Wichita, Kansas, USA) camera comprising multispectral (MS), panchromatic (PAN), and thermal sensors. The MS and PAN cameras have resolutions of 2064 × 1544 pixels (MS) and 4112 × 3008 pixels (PAN), with focal lengths of 8 mm and 16.8 mm, respectively. The spectral bands include blue (central wavelength 475 nm, full width at half maximum (FWHM) 32 nm), green (560 nm, 27 nm), red (668 nm, 14 nm), red-edge (717 nm, 12 nm), near-infrared (842 nm, 57 nm), and a panchromatic band (643.5 nm, 463 nm). The thermal sensor operates in the 7.5–13.5 µm range with a resolution of 640 × 512 pixels for surface temperature measurements.

The UAS is equipped with an integrated Applanix APX-15 EI UAV a dual-frequency L1/L2 GNSS receiver and dual inertial measurement units (IMU), which provides high-accuracy positioning and orientation for precise georeferencing of the imagery. The UAS is connected to an external GNSS correction service that provides real-time accuracy improvements for precise kinematic positioning. Alternatively, post-processed kinematic (PPK) solution can be calculated after the flight using the GNSS base station data. In this study, UAS was connected to the Finnish FINPOS GNSS reference network, which supplies real-time kinematic (RTK) correction; and additionally, the FINPOS reference data from the closest station was loaded for the post-processing. The specifications for the Applanix APX-15 EI UAV performance include position accuracy of 2-5 cm in RTK and post-processed, roll and pitch accuracy of 0.03° in RTK and 0.025° in post-processed, and heading accuracy of 0.18° in RTK and 0.08° in post-processed.

The system is controlled remotely through a cloud-based user interface (Figure 2). A local pilot, if required by mission permissions, can also use a traditional RC controller as a back-up C2 link. The flight paths are designed according to regular photogrammetric principles. The drone has an operating time of maximum 20 min.

The system includes autonomous take-off and landing capabilities to support fully automated mission execution. Just before the take-off, the position of drone inside the docking station is recorded using GNSS observations. During the landing phase, the drone navigates towards the docking station using GNSS-based positioning and descents to a predefined altitude above the expected docking station location. If the visual marker inside the docking station is detected by drone’s downward facing landing camera, the drone establishes visual tracking of the marker and uses visual positioning to guide the final landing phase. Prior to the marker detection, the drone relies on GNSS positioning. If the marker is not detected immediately, the drone starts an automated search pattern, that follows a gradually expanding square trajectory, moving horizontally centered on the recorded docking station coordinates. The reliability of the marker detection depends heavily on the accuracy of the GNSS-derived position estimate, especially in the vertical component. Errors in GNSS positioning during the take-off and landing may result in incorrect estimation of the altitude between the drone and the docking station. Thus, the visual marker may appear wrong size or outside the camera field of view, preventing successful detection of the marker.

The system is integrated to the FGI Drone Cloud platform, built on the CSC - Finnish IT Center for Science cloud services (Figure 2). Specifically, the drone is configured to upload automatically after the flight the collected data to a S3 databucket stored on the CSC Allas service. A typical 15 min mission produces a total of 16 GB of data, which takes approximately 90 min to transfer to cloud over 4G mobile data connection. Once the raw data is on cloud, it can be further processed and analysed using either automated cloud computing pipelines or downloaded locally for manual processing.

Figure 1. Rumble Tools Skynest with KB-Drone. The drone is with customised Micasense Altum-PT payload.

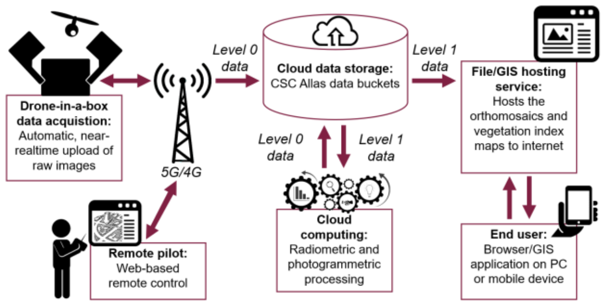

Figure 2. Real-time cloud processing architecture for the multispectral image data in the FGI Drone Cloud platform..

2.2 Flight permissions

Under the European Union Aviation Safety Agency (EASA) regulatory framework, Open category operations are restricted to visual line of sight (VLOS) and are limited to sparsely populated areas in A3 subcategory. BVLOS operations fall under the Specific category and require a Specific Operations Risk Assessment (SORA), typically achieving SAIL II with appropriate mitigations in sparsely populated areas. EASA has prepared Predefined Risk Assessments (PDRA), that cover some BVLOS operations. The PDRAs require that the pilot has VLOS to the UAS during takeoff and landing, preventing operations where the UAS and the pilot are not at the same location. Fully remote operations without onsite pilot monitoring generally require higher risk mitigation levels, significantly increasing technical and procedural requirements. Even these operations require that the pilot is remotely monitoring the flight and has access to flight data, video stream from the UAS, capability to restrict or monitor access to the takeoff/landing site and is able to give commands to the UAS for evasive maneuvers or terminate the flight.

The flights presented in this paper were monitored onsite, as the SORA process for remote operation was not completed. The

https://doi.org/10.5194/isprs-archives-XLIX-B2-2026-1161-2026

SORA has since been finalised, enabling fully remote operations from the office.

2.3 Geometric system calibration

Calibration and field testing of the system was conducted in the Sjökulla calibration site. The calibration flights were conducted on 14.10.2025 to determine the system parameters, including the camera interior orientations (IOPs), lever arms, and the boresight misalignment. They were performed at 6 m/s flight speed using two altitudes, 50 m and 80 m. At each altitude, a single-direction nadir grid was flown with 80% forward and 80% side overlap. The two grids were oriented approximately orthogonally, forming a cross-grid configuration, that resulted in a highly redundant multi-directional image block, with each ground point observed in more than nine images across the two altitudes (Figure 3a).

16 ground control points (GCPs) were installed in the test field area and measured with RTK GNSS receiver with an accuracy of 6.4 mm horizontally and 12.24 mm vertically.

Processing was carried out in Agisoft Metashape Professional (v2.2.0; Agisoft LLC, St. Petersburg, Russia). The software applies Structure-from-Motion (SfM) photogrammetry to estimate both the interior orientation parameters (IOPs) and exterior orientation parameters (EOPs) of the images while simultaneously generating a sparse point cloud. Camera self-calibration was enabled during processing, including the estimation of focal length (f), principal point coordinates (cx, cy), radial distortion coefficients (k1, k2, k3), tangential distortion coefficients (p1, p2), and the affinity coefficient (b1). Image alignment was performed at high accuracy with a limit of 120,000 key points per image, no tie point limit, and reference-based image pair preselection using post-processed GNSS coordinates. The GCPs were manually marked in at least six images per point, with assigned accuracies of ±0.005 m for GCP coordinates and ±0.05 m and 0.5° for image position and orientation observations, respectively. The sparse point cloud was filtered using Metashape's gradual selection tools based on reprojection error and reconstruction uncertainty criteria, complemented by minor manual removal of visually identified outliers. Approximately 10% of the least reliable points were removed from each dataset during the combined filtering process. After filtering, camera parameters and sparse point coordinates were refined in Metashape using the camera optimization function, including estimation of boresight rotations and lever-arm offsets between the navigation system and the camera.

2.4 Validation method

For the validation, the system was operated in the regular mapping mode from the flight height of 80 m on 17 June 2025 and 14 October 2025 in the Sjökulla test field (Figure 3b) and on 15 October 2025 in a forest test area (Figure 3c). The output products were calculated with direct georeferencing mode (DG) and with post-processed georeferencing mode (PPG). In the former, the point coordinates, orthophotos, and point clouds were calculated by using the system calibrations and directly measured image orientations, while in the case of PPG, a full bundle block adjustment was calculated before output product generation. In this study, the PPK GNSS/IMU solution was used.

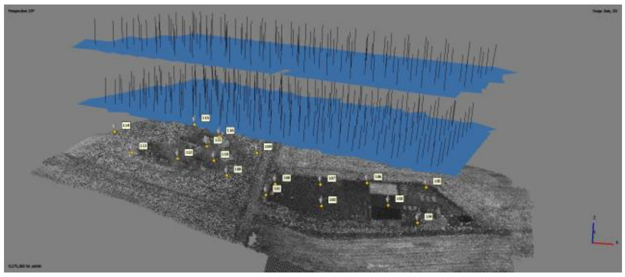

(a)

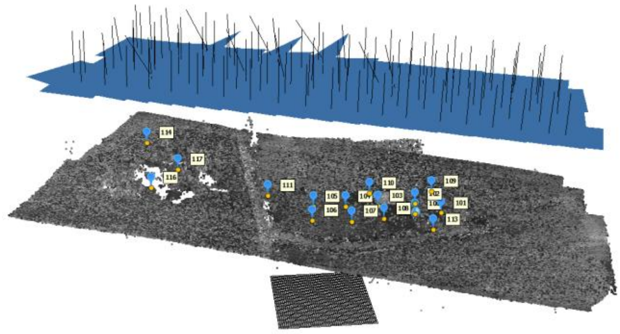

(b)

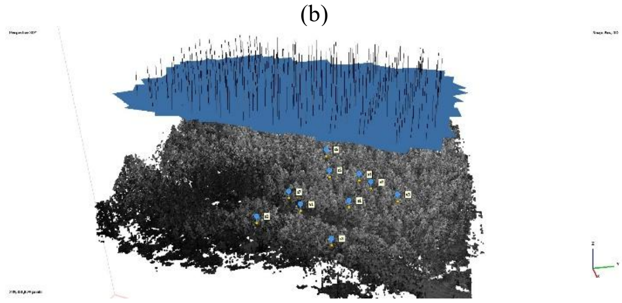

(c)

Figure 3. (a) Calibration flight setup in Sjökulla test field from 14 October 2025. (b) Validation flight setup in Sjökulla test field from 17 June 2025. (c) Validation flight setup in forest test area from 15 October 2025.

The geometric performance of the DiaB mapping system was evaluated using a multi-level validation framework integrating absolute accuracy assessment, temporal consistency analysis, and structural comparison against independent reference data:

1. Absolute accuracy was assessed by comparing photogrammetrically derived point positions against previously surveyed checkpoints, 16 in the Sjökulla test field and 10 in the forest validation area. Positional differences were evaluated using RMSE metrics in the horizontal (X, Y), vertical (Z), two-dimensional (2D), and three-dimensional (3D) accuracy components.
2. Temporal consistency and repeatability were evaluated through DSM differencing of repeated UAV acquisitions collected over the same area. DSMs were aligned on a common grid, and elevation differences were analyzed in locations expected to remain unchanged between epochs. This analysis quantified the stability of the workflow and its suitability for time-series monitoring and change-detection applications.
3. Forest-structure reconstruction quality was examined through visual and structural comparison with an independent UAS LiDAR dataset collected over the forest validation site. The comparison focused on canopy-height representation, terrain consistency, and the spatial distribution of reconstructed points within the forest interior, complementing the quantitative

https://doi.org/10.5194/isprs-archives-XLIX-B2-2026-1161-2026 | © Author(s) 2026. CC BY 4.0 License.

GCP-based assessment with insight into the realism and robustness of the derived three-dimensional forest geometry.

Together, these validation components provide a comprehensive assessment of system performance, covering absolute positional accuracy, temporal stability, and structural consistency across different environments and acquisition scenarios.

3. Results and Discussion

3.1 Overall behaviour of the system

Across the calibration and validation flights (14.10, 17.06, 15.10), the RumbleTools Skynest system demonstrated stable and reliable performance, successfully executing fully autonomous take-offs, mission flights, and returns to the docking station without operational disturbances. Consistent and accurate docking was achieved when high-quality GNSS positioning was established prior to take-off. Earlier test campaigns have showed that insufficient GNSS initialization can negatively affect the visual landing phase, leading to incorrect approach height and failure to detect the docking markers. These observations are consistent with the system's operational principle, in which precise landing relies on the combined use of GNSS-based navigation and vision-based alignment during the final descent.

3.2 System calibration

The boresight and lever arm parameters and their estimated standard deviations are presented in Table 1. Results indicate that across the two independent calibration flights and the combined block, the lever-arm had good repeatability in the horizontal plane, giving standard deviation of 0.15 cm and 0.19 cm for X and Y, respectively, and moderate repeatability in the vertical direction, with a standard deviation 3.38 cm for Z. The boresight angles were stable, with standard deviation of 0.013°, 0.0049°, and 0.0022° for yaw, pitch and roll, respectively. These values indicate well-conditioned and repeatable calibration geometry.

Camera interior orientation parameters obtained from the two calibration flights, their combined data and validation flights PPG-PPK are summarized in Table 2. Principal distance values were highly consistent in three calibration datasets, slightly higher in flight 2 than the others. However, lever-arm vertical direction was smaller in flight 2, which indicates correlation between principal distance and lever-arm vertical direction calibration. There were only small variations in principal point coordinates and distortion coefficients. The stability of the interior parameters confirms the robustness of the camera model across independent flights.

3.3 Validation in Sjökulla test field

The test field validation flights conducted on 17 June 2025 demonstrated consistent and clearly distinguishable performance between the DG and bundle-adjusted workflows (Table 3). The DG-PPK configurations resulted in 3D RMSE values of 43.46 cm, reflecting the expected accuracy level achievable without image-based geometric constraints. In contrast, the PPG-PPK solution achieved significantly better accuracy, with 3D RMSE values of 3.93 cm. These results indicate that while the direct georeferencing approach provides sufficient accuracy for many operational applications, the bundle-adjusted workflow is required when centimeter-level precision is needed.

#F	Lx	Ly	Lz		dw	dw	dk
1	-3.95	0.46	16.34		88.75	-0.58	0.30
2	-3.68	0.10	10.97		88.72	-0.57	0.30
1+2	-3.69	0.22	17.22		88.73	-0.57	0.30
Std	0.15	0.19	3.38		0.0129	0.0049	0.0022

Table 1. Calibration parameters and standard deviations from the 14 October 2025 calibration flight. Lever-arms (Lx, Ly, Lz) are given in centimeters, and boresight angles (dw, dj, dk) are given in degrees. #F: flight number.

	calib 1	calib 2	calib 1&2	Val. PPK
f	2283.356	2284.83	2282.655	2282.655
cx	4.856799	4.52785	4.645546	4.510318
cy	-9.2742	-9.32023	-9.33832	-8.44402
k1	-0.12807	-0.12789	-0.12783	-0.12731
k2	0.166667	0.165477	0.165283	0.164943
k3	-0.05186	-0.0492	-0.04949	-0.05036
p1	0.000113	0.000115	0.000109	0.000143
p2	0.000237	0.000225	0.000225	0.000218
b1	-0.1035	-0.14394	-0.10999	-0.15997

Table 2. Camera interior parameters from the calibration flight conducted on 14 October 2025 and the validation flight conducted on 17 June2025. Listed parameters include principal distance (f), principal point coordinates (cx, cy), radial (k1, k2, k3) and tangential lens distortions (p1, p2), and affinity coefficient (b1).

	RMSE (cm)				
	X	Y	Z	2D	3D
DG-PPK-TF	32.72	27.44	8.04	42.71	43.46
PPG-PPK-TF	1.92	2.24	2.59	2.95	3.93
DG-PPK-forest	12.67	17.57	11.14	21.66	24.36
PPG-PPK-forest	2.16	1.92	6.27	2.89	6.91

Table 3. Accuracy results (RMSE, cm) for direct georeferencing (DG) and post-processed georeferencing (PPG) for flights conducted in the test field on 17 June 2025 and in the forest on 15 October 2025.

Visual inspection of the DSM difference map between 17 June 2025 and 14 October 2025 indicates that elevation discrepancies between the two acquisition epochs remain predominantly close to zero in areas without physical change (Figure 4). Stable surfaces, such as bare ground, infrastructure, and non-vegetated terrain, exhibit differences below a few centimeters, appearing as neutral (white) tones in the color-coded difference map. This pattern reflects strong temporal consistency between datasets and suggests that the applied post-processed bundle block adjustment, incorporating PPK positioning together with calibrated lever-arms, boresight parameters, and interior orientation, achieves robust geometric alignment without GCPs. The observed stability demonstrates that the workflow produces repeatable surface models suitable for reliably detecting structural changes within forested environments.

https://doi.org/10.5194/isprs-archives-XLIX-B2-2026-1161-2026

The orthomosaic shows good geometric consistency; however, its radiometric quality is affected by varying illumination conditions, including changes in sunlight and cloud cover (Figure 5a).

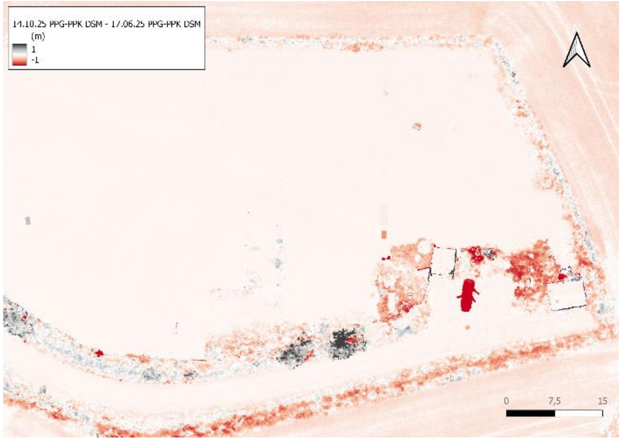

Figure 4. DSM difference map computed from PPG-PPK reconstructions between 17 June 2025 and 14 October 2025.

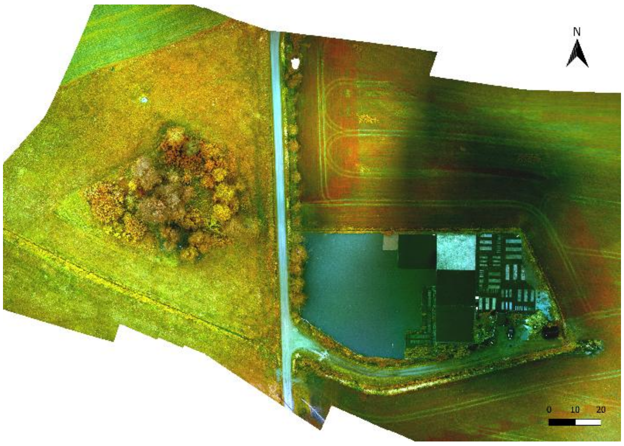

(a)

(b)

Figure 5. (a) Orthomosaic of the test field from 17 June 2025. (b) Orthomosaic of the forest test area from 15 October 2025.

3.4 Forest validation flights

The forest validation flights showed similarly consistent performance across the evaluated processing workflows. When compared against the ground-truth GCPs (Table 3), the DG-PPK configuration achieved a 3D RMSE of 24.36 cm, while the BBA-PPK workflow resulted in a 3D RMSE of 6.91 cm. Although the forest environment is structurally more complex than the open test field, the direct georeferencing solution performed comparatively better here than in the test field experiment, yielding noticeably lower RMSE values. This indicates that under the conditions present during the forest validation flight, the DG-based solution maintained a level of geometric consistency that may be sufficient for applications tolerating decimeter-level accuracy. Nevertheless, the bundle-adjusted workflow continued to provide the highest accuracy, reducing vertical and 3D residuals to the centimeter scale and thereby offering improved reliability for detailed forest structure analysis.

Visual comparison with the reference UAV LiDAR point cloud indicates excellent geometric agreement between the photogrammetric reconstructions and the LiDAR-derived canopy and terrain surfaces within the forested validation area (Figure 6). Both workflows successfully reproduce the dominant canopy structure and ground elevation, demonstrating that nadir multispectral imagery can reliably capture forest geometry under typical operational conditions. However, as expected for image-based reconstruction in dense forest environments, fine-scale trunk geometry and understory elements are less distinctly represented compared to the LiDAR reference.

Differences between the two processing strategies are evident in the resulting point cloud characteristics. The bundle-adjusted reconstruction (PPG-PPK) yields a smoother and more spatially coherent point distribution (Figure 6a), whereas the direct georeferencing solution (DG-PPK) exhibits locally increased point dispersion and isolated noise points (Figure 6b). This behavior reflects the additional geometric constraints introduced through image tie points in the bundle adjustment, which enhance internal consistency and reduce reconstruction noise. Overall, both approaches produce geometrically consistent forest representations, while the bundle-adjusted workflow provides improved stability and fidelity for detailed structural analysis.

The evaluation results demonstrate that the customized DiaB mapping system provides robust and reliable geometric performance for autonomous UAV operations. Accuracy assessments against GCPS confirm that centimeter-level 3D positioning accuracy is consistently achieved when post-processed georeferencing (PPG) is applied. In contrast, DG yields lower accuracy, though the attained decimeter-level performance remains suitable for a range of operational mapping tasks where high relative accuracy is sufficient.

Temporal validation using DSM differencing further confirms the geometric stability of the system. Repeated acquisitions collected four months apart show elevation differences on the order of a few centimeters in stable, non-changing terrain. This level of agreement demonstrates strong temporal consistency between epochs and indicates that the workflow produces repeatable surface models suitable for time-series analysis and change-detection applications.

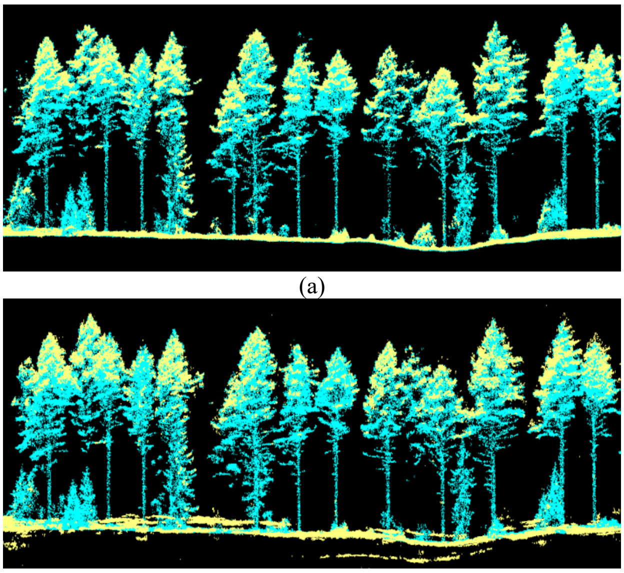

(a)

(b)

Figure 6. Top: Forest validation flight photogrammetric point cloud point cloud (yellow) shown together with the reference UAV LiDAR point cloud (blue), (a) processed with PPG-PPK, and (b) with DG-PPK.

Additional assessment in forested environments, based on comparisons with reference UAV LiDAR data, shows good agreement in canopy and terrain structure. Both processing strategies reconstruct the main forest geometry, while the bundle-adjusted PPG workflow provides enhanced internal consistency and reduced noise, enabling reliable use in structurally complex environments.

Overall, the results highlight the critical role of rigorous system calibration, including lever-arm estimation, boresight alignment, and camera interior orientation, in ensuring geometric reliability and repeatability across diverse environments and acquisition conditions. The demonstrated performance confirms that the presented system and processing pipeline form a capable and practical foundation for automated, high-frequency forest monitoring. Future work will focus on extending the approach to long-term time series, integrating forest structural and biomass metrics, and deploying multi-site autonomous monitoring installations.

4. Conclusion

This study validated the geometric performance of a novel multispectral DiaB remote sensing system. The system was capable of achieving cm-level multitemporal accuracy without in situ ground control points, both in a controlled test field environment and in a forestry application, provided that bundle block adjustment was applied as part of the processing workflow. However, the precision of direct georeferencing was limited, resulting in decimetre-level accuracy at a flight altitude of 80 m. At present, the main limitation of the system is the relatively slow data transfer between the UAS and the cloud computing platform, which restricts its use in real-time decision support applications. Future studies should also develop quantitative radiometric processing chain for the system.

Acknowledgements

This research was funded by the Academy of Finland within project "Autonomous drone solutions for single tree-based forest management" (decision no. 359404). This study has been performed with affiliation to the Academy of Finland Flagship Forest–Human–Machine Interplay—Building Resilience, Redefining Value Networks and Enabling Meaningful Experiences (UNITE) (decision no. 357908). The authors acknowledge CSC – IT Center for Science for providing cloud resources, including Allas Object Storage, used in this work.

During the preparation of this work, the authors used ChatGPT and Microsoft Copilot for enhancing readability and language. After using these tools, the authors reviewed and edited the content as needed and take full responsibility for the content of the published article.

References

Alexandre, R. C. J., Martins, L. E. G., Gorschek, T., 2023. Cybersecurity Risk Assessment for Medium-Risk Drones: A Systematic Literature Review. *IEEE Aerospace and Electronic Systems Magazine* 38(6), 28–43. https://doi.org/10.1109/MAES.2023.3251969

Cheng, M.-L., Matsuoka, M., Liu, W., Yamazaki, F., 2022. Near-real-time gradually expanding 3D land surface reconstruction in disaster areas by sequential drone imagery. *Automation in Construction* 135, 104105. https://doi.org/10.1016/j.autcon.2021.104105

Hinzmann, T., Schönberger, J. L., Pollefeys, M., Siegwart, R., 2017. Mapping on the Fly: Real-Time 3D Dense Reconstruction, Digital Surface Map and Incremental Orthomosaic Generation for Unmanned Aerial Vehicles. *Springer Proceedings in Advanced Robotics* 383–396. Springer International Publishing. https://doi.org/10.1007/978-3-319-67361-5_25

Jiang, S., Jiang, C., Jiang, W., 2020. Efficient structure from motion for large-scale UAV images: A review and a comparison of SfM tools. *ISPRS Journal of Photogrammetry and Remote Sensing* 167, 230–251. https://doi.org/10.1016/j.isprsjprs.2020.04.016

La Salandra, M., Nicotri, S., Donvito, G., Italiano, A., Colacicco, R., Miniello, G., Lapietra, I., Roseto, R., Dellino, P., Capolongo, D., 2024. A paradigm shift in processing large UAV image datasets for emergency management of natural hazards. *International Journal of Applied Earth Observation and Geoinformation* 132, 103996. https://doi.org/10.1016/j.jag.2024.103996

Nex, F., Armenakis, C., Cramer, M., Cucci, D. A., Gerke, M., Honkavaara, E., Kukko, A., Persello, C., Skaloud, J., 2022. UAV in the advent of the twenties: Where we stand and what is next. *ISPRS Journal of Photogrammetry and Remote Sensing* 184, 215–242. https://doi.org/10.1016/j.isprsjprs.2021.12.006

Schwarz, K., Champman, M., Cannon, M., Gong. P., 1993. An integrated ins/gps approach to the georeferencing of remotely sensed data. *Photogramm. Eng. Remote. Sens.* 53(1993), 1667-1674.